INORGANIC CHEMISTRY
FRONTIERS

RESEARCH ARTICLE

View Article Online
View Journal | View Issue

Cite this: *Inorg. Chem. Front.*, 2025, **12**, 1918

Tunable luminescent lanthanide cluster-based hydrogel probe for ratiometric detection of ofloxacin, anti-counterfeiting, and magnetocaloric applications†

Tian-Tian Wang, Hao Wang and Wen-Bin Sun *

Received 6th December 2024,
Accepted 12th January 2025

DOI: 10.1039/d4qi03133d

rsc.li/frontiers-inorganic

Misuse and overuse of antibiotics, especially Ofloxacin (OFX), have become significant global health concerns, emphasizing the urgent need for efficient and accessible detection methods. To address this issue, a series of Ln_{14} clusters, formulated as $[Ln_{14}(acac)_{24}(\mu_4\text{-}OH)_2(\mu_3\text{-}OH)_{16}]\cdot C_6H_{14}$ (Ln^{III} = Gd^{III} (**Gd_{14}**), Tb^{III} (**Tb_{14}**), Eu^{III} (**Eu_{14}**) and Sm^{III} (**Sm_{14}**)) (Hacac = acetylacetone), were successfully synthesized using the Hacac ligand and lanthanide salts in this work. Among these, **Gd_{14}** exhibits typical magnetocaloric effect behavior with the $-\Delta S_m^{max}$ of 39.58 J kg^{-1} K^{-1} and more importantly, a ratiometric luminescent probe based on **Tb_9Eu_5** by co-doping Tb^{III} and Eu^{III} ions was found enabling visual detection and reusable sensing of OFX in tap water. This marks the first application of lanthanide clusters in ratiometric luminescent detection of OFX. Further to expand the practical applications of this material, a composite film sensor was prepared by incorporating the cluster with carrageenan hydrogel, facilitating visual detection of OFX and anti-counterfeiting. The results demonstrate that the sensor possesses excellent sensitivity for OFX detection and can achieve multi-layered anti-counterfeiting through simple cutting and assembly.

Introduction

At the dawn of the 20th century, antibiotics revolutionized medicine, saving countless lives from bacterial infections. However, their misuse and overuse have led to significant health risks and escalated antibiotic resistance, turning it into a major global public health threat.[1,2] Ofloxacin, a fluoroquinolone antibiotic, is widely used to treat respiratory, urinary, and soft tissue infections due to its broad-spectrum efficacy. However, its widespread use leads to environmental and health risks, as unmetabolized OFX contaminates water sources, affects aquatic life, and promotes the spread of antibiotic resistance genes, which may impact human health through the food chain.[3,4] Current OFX detection methods, such as high-performance liquid chromatography (HPLC) and mass spectrometry (LC-MS), require expensive equipment and complex procedures, limiting their ability for real-time, high-sensitivity detection.[5–7] Therefore, developing a simple, rapid, and highly sensitive method to detect low concentrations of OFX in environmental samples is crucial.

Ratiometric luminescent probes, due to their high sensitivity, excellent selectivity, and capability for real-time monitoring, are expected to be an alternative method for the detection of ofloxacin and other antibiotics.[8–10] Their main advantage lies in the ability to generate multiple luminescence signals at different wavelengths simultaneously, allowing for intensity ratio analysis, eliminating background interference, and enhancing detection accuracy and sensitivity. Lanthanide clusters have attracted considerable attention in probe design due to their unique optical properties.[11–15] Lanthanide ions exhibit high luminescence efficiency, long luminescence lifetimes, and narrow emission bands, all of which improve probe performance. Furthermore, the emission spectra of lanthanide clusters possess strong tunability, enabling the generation of dual-wavelength emission signals that improve detection accuracy in complex systems. By modulating these luminescent properties, multi-color emission can be generated, providing distinctive optical markers for anti-counterfeiting applications.[16] Moreover, integrating lanthanide clusters with flexible materials like carrageenan hydrogels allows the development of functional composites that preserve optical properties while enhancing mechanical strength and environmental stability, broadening their applicability in real-time detection

Key Laboratory of Functional Inorganic Material Chemistry Ministry of Education, School of Chemistry and Material Science Heilongjiang University, 74 Xuefu Road, Harbin 150080, P. R. China. E-mail: wenbinsun@126.com

†Electronic supplementary information (ESI) available: Selected bond lengths (Å) and angles (°), the Gd^{III} geometry analysis, IR, PXRD patterns, analysis of frontier molecular orbitals, magnetic data and luminescence properties for complexes. CCDC 2403575. For ESI and crystallographic data in CIF or other electronic format see DOI: https://doi.org/10.1039/d4qi03133d

and anti-counterfeiting.[17–20] Additionally, lanthanide clusters, especially those with Gd^{III} ions, exhibit significant magnetocaloric effects, making them strong candidates for efficient and environmentally friendly cooling devices.[21–24]

Drawing on the unique optical properties of lanthanide clusters in probe design, acetylacetone (Hacac) has shown promise as an effective ligand for enhancing the stability and luminescent performance of lanthanide luminescent complexes.[25,26] As a typical β-diketone ligand, Hacac forms stable chelates with lanthanide ions through its two carbonyl oxygen atoms, improving complex stability. Additionally, Hacac exhibits an "antenna effect", efficiently transferring light energy to lanthanide luminescent centers, boosting luminescence efficiency, especially in Eu^{III} and Tb^{III} complexes. It also reduces non-radiative transition losses, extending the luminescence lifetime, which is beneficial for applications requiring long-term stable signals. Furthermore, the lightweight and multidentate Hacac ligand may potentially generate lanthanide complexes with low M_W/N_M (M_W = molecular weight, N_M = number of metal ions), exhibiting pronounced magnetocaloric effects, thus offering potential applications in magnetic refrigeration.[27,28]

Building upon the research context, this paper reports a series of tetradecanuclear lanthanide clusters with highly symmetrical three-layer double sandwich structure. Among these, **Tb_{14}** exhibits high stability and long luminescence lifetime, with high selectivity, low detection limit, and rapid response toward OFX in tap water. Leveraging the comparable ionic radii and coordination chemistry inherent to lanthanide ions, a series of bimetallic materials, Tb_XEu_{14-X}, has been strategically designed to enable tunable multicolor emissions. Remarkably, **Tb_9Eu_5**, as a distinguished representative of this series, marks the first lanthanide cluster-based ratiometric luminescent probe for the detection of OFX, demonstrating a detection limit of 4.0 μM, which is competitive compared to other reported probes. To validate real-time detection capability, the multicolor emission properties of Tb_XEu_{14-X} were combined with the flexibility of carrageenan hydrogel, resulting in Tb_XEu_{14-X}@CRG functional composite hydrogel sensors with high sensitivity for OFX. Additionally, two anti-counterfeiting strategies were proposed, further demonstrating the broad application prospects of this material. Notably, **Gd_{14}** shows a magnetic entropy change of 39.58 J kg^{-1} K^{-1} in magnetic studies, highlighting the potential of lanthanide clusters in multifunctional materials.

Experimental section

Materials and methods

All complexes were synthesized using readily available chemicals and solvents, without the need for further purification. A PerkinElmer 2400 analyzer was used to determine the elemental composition (C, N, and H) during the experiments. The complexes' magnetic properties were investigated using a quantum-designed VSM SQUID magnetometer. Diamagnetic corrections were applied to the measured data, utilizing Pascal's constants and accounting for the contribution of the sample holder.[29] The luminescence properties of the complexes were investigated at room temperature using an FLS1000 spectrophotometer (Edinburgh Instruments, UK). The crystal structure of **Gd_{14}** was analyzed at 273.15 K using an Xcalibur Eos diffractometer with a wavelength of 0.71073 Å. The structure was refined using the F^2 full-matrix least-squares method with the software packages SHELXTL-2015 and Olex2.[30] The infrared spectra of the complexes in KBr particles were recorded in the region of 4000–500 cm^{-1} using a Nicolet Impact 410 spectrometer (Thermo Fisher, USA).

Synthesis of $[Ln_{14}(acac)_{24}(\mu_4\text{-}OH)_2(\mu_3\text{-}OH)_{16}]\cdot C_6H_{14}$ (Ln^{III} = Gd^{III} (Gd_{14}), Tb^{III} (Tb_{14}), Eu^{III} (Eu_{14}) and Sm^{III} (Sm_{14}))

The synthesis method of the complexes was modified based on previously reported procedures.[26] In this study, we synthesized a series of lanthanide clusters, including the new clusters **Gd_{14}** and **Sm_{14}**, with reference to the previously reported **Eu_{14}** and **Tb_{14}** clusters. The newly synthesized **Gd_{14}** and **Sm_{14}** clusters are isostructural with the previously reported **Eu_{14}** and **Tb_{14}** clusters. As an example for **Gd_{14}**, 0.2 mmol of $NH_3\cdot H_2O$ (0.007 g) and 0.2 mmol of Hacac (0.020 g) were sequentially added to 2 mL of water and stirred for 10 minutes. The resulting mixture was gradually introduced into 10 mL of cold water containing 0.1 mmol of $GdCl_3\cdot 6H_2O$ (0.037 g), while maintaining the pH between 7.0 and 7.5. A white precipitate formed, and the reaction mixture was stirred for an additional 5 hours to ensure completeness. The precipitate was then filtered, washed thoroughly with water to remove residual impurities, and dried in a desiccator. Finally, recrystallization using n-hexane yielded colorless **Gd_{14}** crystals with a yield of 0.13 g (37% based on Gd). IR data (KBr, cm^{-1}): 3480 (m), 2917 (w) 1616 (s), 1517 (s), 1385 (s), 1260 (s), 1015 (s), 920 (s), 761 (m). Elemental analyses calc (%) for $C_{126}H_{200}Gd_{14}O_{66}$: C 30.44, H 4.05; found: C 30.52, H 3.96.

Results and discussion

Description of crystal structure

Analysis from single-crystal X-ray diffraction reveals that the crystal structure of **Gd_{14}** comprises a centrosymmetric octahedral Gd_6 unit and two symmetric tetrahedral Gd_5 units, with the Gd_6 octahedron sharing two opposite vertices with the Gd_5 tetrahedra, forming a highly symmetrical three-layer double sandwich structure[31] (Fig. 1 and Fig. S3†). This vertex-sharing coordination leads to a stable polynuclear structure. In each Gd_5 unit, the Gd_4 square plane is rotated by 45° relative to the Gd_4 square plane in the central Gd_6 unit (Fig. 1d). The asymmetric unit comprises three deprotonated acetylacetone ligands, three Gd^{III} ions, one μ_4-OH group and three μ_3-OH groups (Fig. S4†). All Gd^{III} ions are eight-coordinated, with Gd1 exhibiting a D_{4d} geometry and Gd2 and Gd3 adopting a C_{2v} geometry (Fig. S5† and Table S4†). The ligands exhibit two distinct coordination modes: 16 ligands are terminally che-

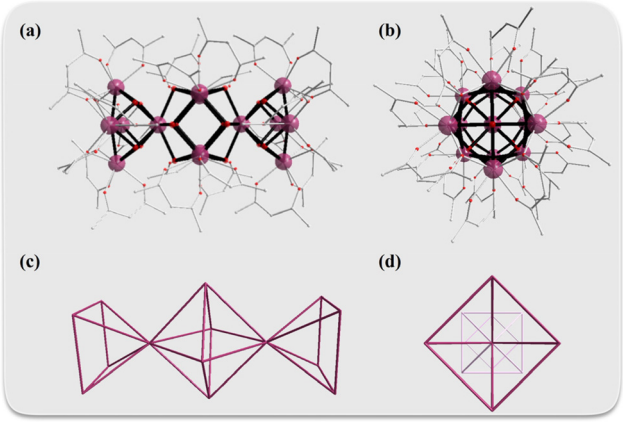

Fig. 1 (a) and (b) molecular structure, (c) and (d) metal core topology for **Gd$_{14}$**. Color code: Gd (plum), O (red), C (grey). H atoms were omitted for clarity.

lated, while 8 acts as bridging chelates (Fig. S6†). The Gd–O bond lengths range from 2.317(5) to 2.651(11) Å, and the distances between adjacent Gd^{III} atoms vary from 3.609 to 3.991 Å. Notably, the Gd–Gd distances within the octahedral Gd_6 unit are longer than those in the tetrahedral Gd_5 units. Table S1† summarizes the crystallographic experimental data of **Gd$_{14}$**, while the selected bond lengths and bond angles of **Gd$_{14}$** are listed in Tables S2 and S3,† respectively. The infrared and XRD spectra of clusters are shown in Fig. S1 and S2.†

Magnetic properties

Gadolinium ion, with its half-filled 4f electronic configuration, high-spin ground state (S = 7/2), and nearly isotropic magnetic properties, is an ideal candidate for efficient magnetocaloric refrigeration materials. The magnetocaloric effect of the polynuclear **Gd$_{14}$** structure has been thoroughly investigated to evaluate its potential applications in magnetic refrigeration.

Initially, the direct current (dc) magnetic susceptibility of **Gd$_{14}$** was measured under a 500 Oe dc magnetic field over a temperature range of 2 to 300 K. At 300 K, the $\chi_M T$ value of **Gd$_{14}$** is 108.91 cm^3 K mol^{-1}, which is in close agreement with the theoretical value of 110.18 cm^3 K mol^{-1} for 14 isolated Gd^{III} ions (S = 7/2, L = 0, $^8S_{7/2}$, g = 2) (Fig. S7†). With the decrease in temperature, the $\chi_M T$ value of **Gd$_{14}$** gradually decreases in the range of 300 to 50 K, followed by a sharp decline to 48.19 cm^3 K mol^{-1} at 2 K. This pronounced decline suggests the presence of weak intramolecular antiferromagnetic interactions, which dominate the magnetic behavior at low temperatures.[32,33] The χ_M^{-1} *vs.* T plot was fitted using the Curie–Weiss law, yielding two key parameters: θ = −3.17 K and C = 110.01 cm^3 K mol^{-1} (Fig. S8†). The negative value of θ further confirms the presence of antiferromagnetic coupling between the Gd^{III} ions within **Gd$_{14}$**.[34]

Subsequently, the relationship between the magnetization (M) and the applied magnetic field (H) for **Gd$_{14}$** was investigated, as depicted in Fig. S9.† The results indicate that in the low-field region, the magnetization increases rapidly with the applied field, followed by a gradual reduction in the rate of increase. At 7 T, the magnetization reaches saturation, exhibiting a maximum value of 97.13$N\beta$. The magnetization of **Gd$_{14}$** is slightly lower than the theoretical spin-only value for fourteen non-interacting Gd^{III} ions, indicating the presence of weak antiferromagnetic interactions between the metal ions. On the other hand, the non-overlapping nature of the M–H/T curves for **Gd$_{14}$** may be attributed to the pronounced magnetic isotropy of the Gd^{III} ions (Fig. S10†).

To explore the potential magnetocaloric effect behavior of **Gd$_{14}$**, the Maxwell equation can be applied to determine the maximum $-\Delta S_m$ values, expressed as:[35,36]

$$\Delta S_m(T) = \int [\partial M(T,H)/\partial T]_H \mathrm{d}H$$

As the temperature decreases and the applied magnetic field increases, the $-\Delta S_m$ value of **Gd$_{14}$** gradually rises, reaching a maximum of 39.58 J kg^{-1} K^{-1} at T = 2 K and ΔH = 7 T (Fig. 2). This value is lower than the theoretical value of 48.67 J kg^{-1} K^{-1}, calculated using the formula $\Delta S_m = nR\ln(2S+1)$.[37] This discrepancy may be attributed to the presence of antiferromagnetic interactions between the Gd^{III} centers. Although **Gd$_{14}$** possesses a lower nuclearity compared to Gd_{27},[38] Gd_{28},[39] and Gd_{36},[40] its $-\Delta S_m$ value is comparable, underscoring its remarkable potential for application in magnetic refrigeration.

Luminescence properties

Given the unique luminescence properties of lanthanide elements, the photoluminescence characteristics of **Tb$_{14}$**, **Eu$_{14}$** and **Sm$_{14}$** were evaluated at room temperature (Fig. 3a and Fig. S11–S13†). Upon excitation at 335 nm, **Tb$_{14}$** exhibits characteristic sharp emission peaks at 487, 542, 580, and 615 nm, corresponding to the $^5D_4 \rightarrow {}^7F_J$ (J = 6–3) transitions of the Tb^{III} ions. Similarly, in the emission spectrum of **Eu$_{14}$**, the characteristic peaks of Eu^{III} corresponding to the $^5D_0 \rightarrow {}^7F_J$ (J = 0–4) transitions are observed at 574, 587, 608, 648, and 698 nm, respectively. In the emission spectrum of **Sm$_{14}$**, the characteristic peaks of Sm^{III} corresponding to the $^4G_{5/2} \rightarrow {}^6H_J$ (J = 5/2–11/2) transitions are observed at 563, 603, 645, and 709 nm, respectively.

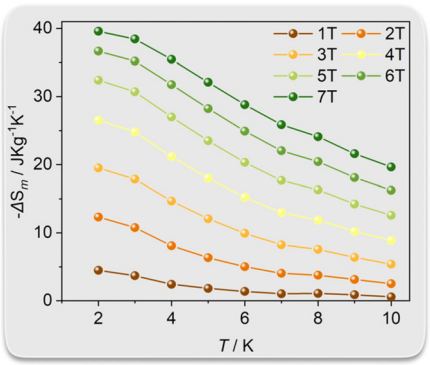

Fig. 2 Plot of experimental magnetic entropy change ($-\Delta S_m$) *versus* T for **Gd$_{14}$**.

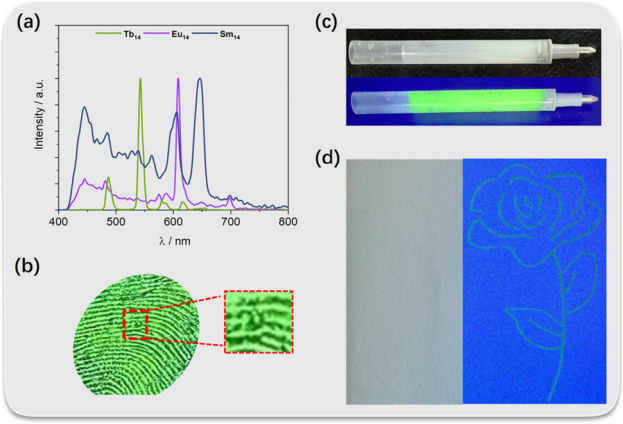

Fig. 3 (a) Excitation and emission spectra of Ln_{14}; (b) luminescence images of potential fingerprints on glass after sprinkling the solid powders of **Tb_{14}** under a 365 nm UV lamp; (c) refills loaded with **Tb_{14}** under daylight (top) and 365 nm UV lamp (bottom); (d) paper after writing under daylight (left) and 365 nm UV lamp (right).

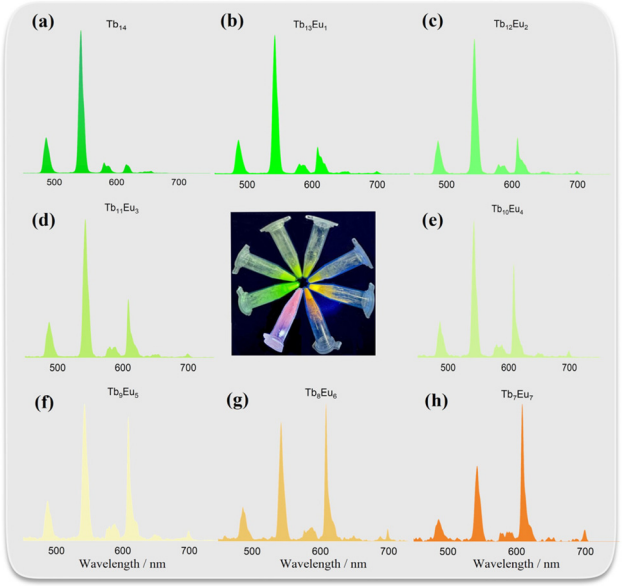

Fig. 4 Emission spectra (λ_{ex} = 335 nm) of **Tb_{14}** (a), **$Tb_{13}Eu_1$** (b), **$Tb_{12}Eu_2$** (c), **$Tb_{11}Eu_3$** (d), **$Tb_{10}Eu_4$** (e), **Tb_9Eu_5** (f), **Tb_8Eu_6** (g), and **Tb_7Eu_7** (h). Inset: photographs of the in Tb_XEu_{14-X} excited with a UV lamp.

The strong luminescence properties of **Tb_{14}** make it a potential candidate for applications in forensic science. By first depositing a volunteer's fingerprint on a glass surface and evenly sprinkling **Tb_{14}** solid powder over it, followed by the gentle removal of excess powder using a rubber bulb, the fingerprint's luminescent image becomes clearly visible under 365 nm ultraviolet light (Fig. 3b). Additionally, **Tb_{14}** suspension in a glycerol–water mixture remains stable for at least one month, making it suitable for use as capillary ink (Fig. 3c). Under ultraviolet light, it emits a bright luminescence (Fig. 3d), demonstrating its potential applications in writing.

To investigate the energy transfer between metal ions within the cluster, heterometallic clusters Tb_XEu_{14-X} were synthesized by doping Eu^{III} into **Tb_{14}** at various molar ratios, with the resulting emission spectra depicted in Fig. 4. The PXRD and IR results indicate that Tb_XEu_{14-X} and **Tb_{14}** are isostructural (Fig. S14 and S15†). In addition, ICP-OES analysis confirms that the metal ratio is consistent with the lanthanide ratio used for synthesis (Table S5†). Furthermore, the EDX mapping confirms the uniform distribution of Eu^{III} and Tb^{III} ions within the bimetallic cluster particles (Fig. S16†). As the Tb^{III}/Eu^{III} ratio decreases, the emission of Tb_XEu_{14-X} gradually shifts from the green emission of Tb^{III} to the red emission of Eu^{III}, thereby achieving tunable luminescence. The corresponding CIE chromaticity diagram is shown in Fig. S17.† To verify the energy transfer process from Tb^{III} to Eu^{III} in the co-doped samples, the luminescence lifetime decay curves of the Tb^{III} ions were measured. Fig. S18 and S19† show that, upon the introduction of Eu^{III}, the luminescence lifetime of Tb^{III} decreases, confirming efficient energy transfer from the excited state of Tb^{III} to Eu^{III}. To verify the generality of this mechanism, we further synthesized two heterometallic clusters containing Sm^{III} and Tb^{III} ions: **$Tb_{10}Sm_4$** and **Tb_4Sm_{10}**. Given the similar emission levels of Sm^{III} and Eu^{III} ions ($^4G_{5/2}$ and 18 000 cm^{-1} for Sm^{III}, $^5D_0$ and 17 200 cm^{-1} for Eu^{III}), energy transfer from Tb^{III} to Sm^{III} is also expected to occur. As shown in Fig. S20,† this phenomenon further demonstrates the versatility of this system.[16]

Luminescence detection of OFX

Considering the excellent stability and strong luminescence performance of Ln_{14}, we initially selected **Tb_{14}** to explore its sensing potential for OFX in tap water suspensions (Fig. 5).

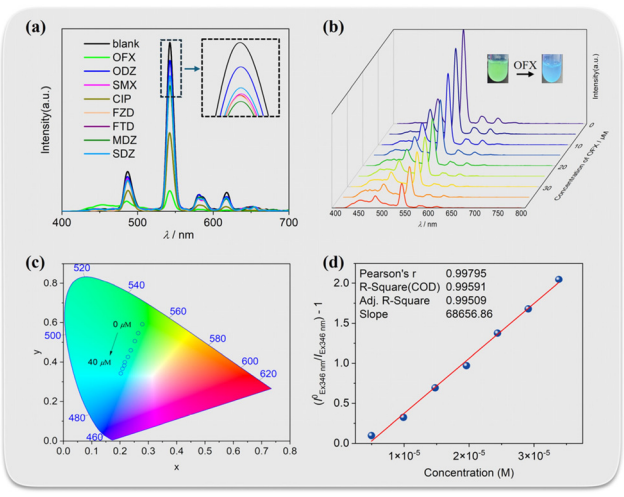

Fig. 5 (a) Luminescence sensing of **Tb_{14}** in diverse antibiotic solutions in tap water (λ_{ex} = 335 nm); (b) luminescence sensing of **Tb_{14}** to OFX in tap water (λ_{ex} = 335 nm). Inset: photographs of **Tb_{14}** in tap-water under the irradiation of a UV lamp (365 nm) before and after addition of 40 μM OFX; (c) CIE coordinates of **Tb_{14}** after addition of different concentrations of OFX; (d) the shape of the relationship between the luminescence intensities of **Tb_{14}** and the concentrations of OFX.

Under excitation at 335 nm, **Tb_{14}** exhibited a significant quenching effect in the presence of OFX, whereas other antibiotics (Scheme S1†), including fluoroquinolone compounds like ciprofloxacin (CIP), resulted in a quenching efficiency of no more than 50%. Even in complex background solutions containing multiple antibiotics, the quenching effect of OFX on **Tb_{14}**'s luminescence remained consistent with that observed in tap water, demonstrating its exceptional selectivity and anti-interference capability (Fig. S21†). Within the low concentration range of 5 to 40 μM, the luminescence intensity showed a linear relationship with the OFX concentration, consistent with the Stern–Volmer equation, yielding a high K_{SV} value of 68 657 M^{-1} and a detection limit as low as 0.44×10^{-6} M.[41,42]

To evaluate the sensing potential of a ratiometric luminescent probe for OFX, we conducted luminescence titration experiments using **Tb_9Eu_5**. The reason for selecting **Tb_9Eu_5** is that for **$Tb_{13}Eu_1$**, **$Tb_{12}Eu_2$**, and **Tb_7Eu_7**, the color change observed with the naked eye during OFX detection is not very pronounced, which may limit their practical application (Fig. S22†). In contrast, for **$Tb_{11}Eu_3$**, **$Tb_{10}Eu_4$**, **Tb_9Eu_5**, and **Tb_8Eu_6**, after adding 100 μM OFX, **Tb_9Eu_5** shows the largest change, with the I_{608nm}/I_{542nm} ratio increasing from an initial 0.85 to 2.34, corresponding to a relative change of 175% (Table S6†). Therefore, **Tb_9Eu_5** is selected as the ratiometric luminescence probe for detecting OFX. Upon excitation at 335 nm, **Tb_9Eu_5** exhibited a characteristic ratiometric luminescence response to OFX in tap water. With the increasing concentration of OFX, the emission of Tb^{III} at 542 nm gradually diminished, while the emission of Eu^{III} at 608 nm became progressively stronger (Fig. 6). This shift led to a distinct color change from yellow to bright red, clearly visible to the naked eye. Within the concentration range of 10 μM to 100 μM, the ratio of intensities (I_{608nm}/I_{542nm}) displayed a linear correlation with OFX concentration, yielding a K_{SV} value of 7565 M^{-1} and a detection limit as low as 4.0 μM (Fig. S23†). Furthermore, selectivity and anti-interference tests confirmed that **Tb_9Eu_5** functions as a rapid and reliable ratiometric luminescent probe for OFX (Fig. S24†). The test results indicate that the detection limit of the ratio luminescent probe **Tb_9Eu_5** is higher than that of the single luminescent probe **Tb_{14}**. This may be attributed to the reliance of the ratio luminescent probe on the energy transfer mechanism between distinct luminescent centers, where the energy transfer efficiency from Tb^{III} to Eu^{III} in the **Tb_9Eu_5** system is likely to be lower, which leads to reduced signal intensity and, consequently, lower sensitivity.

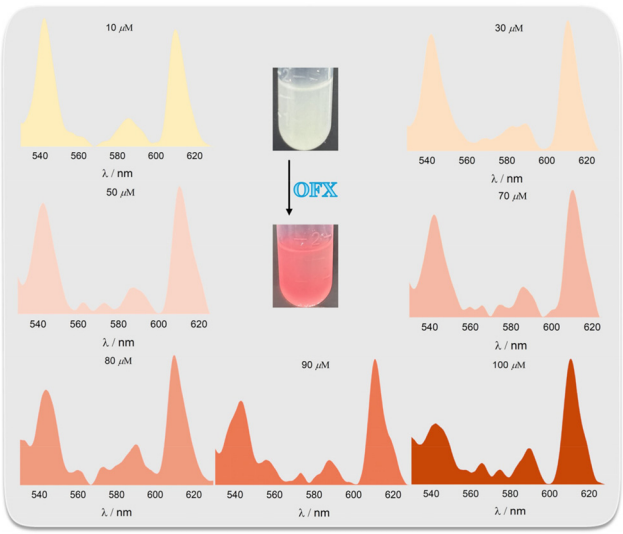

Fig. 6 Luminescence sensing of different concentrations of OFX by **Tb_9Eu_5** in tap water (λ_{ex} = 335 nm). Inset: photographs of **Tb_9Eu_5** in tap-water under the irradiation of a UV lamp (365 nm) before and after addition of 100 μM OFX.

The stability of **Tb_{14}** and **Tb_9Eu_5** in the presence of OFX was further confirmed (Fig. S25†). After exposure to OFX for 3 days, the emission spectra of **Tb_{14}** showed no significant changes, indicating its long-term stability as an OFX sensing material. For **Tb_9Eu_5**, a slight variation was observed in the emission wavelengths between 560 and 600 nm, which could be attributed to environmental factors such as temperature, humidity, or interactions between the ligand and the environment. However, since the comparison was based on the emission intensity ratio of the two peaks at 608 nm and 542 nm for **Tb_9Eu_5**, which remained unchanged, the overall stability of the sample was minimally affected. In addition, **Tb_{14}** and **Tb_9Eu_5** demonstrated excellent recyclability (Fig. S26†). Following the sensing and detection process, the luminescence intensity could be effectively restored through ultrasonic washing and centrifugation, allowing the materials to be reused at least two times. This highlights their potential for sustainable application in real-world scenarios.

To evaluate the detection performance of these clusters in real samples, we selected antibiotics purchased from a pharmacy for testing (Fig. S27†). Upon the addition of 20 mg L^{-1} of ofloxacin, the luminescence intensity of **Tb_{14}** at 542 nm decreased by 79%, while the emission intensity ratio of **Tb_9Eu_5** at 608 nm to 542 nm (I_{608nm}/I_{542nm}) increased from 0.87 to 2.04. These findings confirm the effective detection capabilities of **Tb_{14}** and **Tb_9Eu_5** for OFX in complex matrices, further confirming their potential as reliable sensing materials for practical applications.

To comprehensively investigate the sensing mechanism of **Tb_{14}** towards OFX, we considered the following aspects. Firstly, the PXRD and IR spectra of the complexes post-response showed excellent consistency with the initial spectra (Fig. 7a and b). These results not only indicate that the structural integrity of the complexes remains intact after the identification of the target analyte but also confirm the absence of new coordination or hydrogen bonds between the complexes and OFX. Therefore, the luminescence response is not attributable to structural collapse or coordination and hydrogen-bonding interactions.[43]

Furthermore, as shown in Fig. 7c, there was no overlap between the emission spectrum of **Tb_{14}** and the UV absorption spectrum of OFX, effectively ruling out the possibility of luminescence quenching *via* the Förster resonance energy

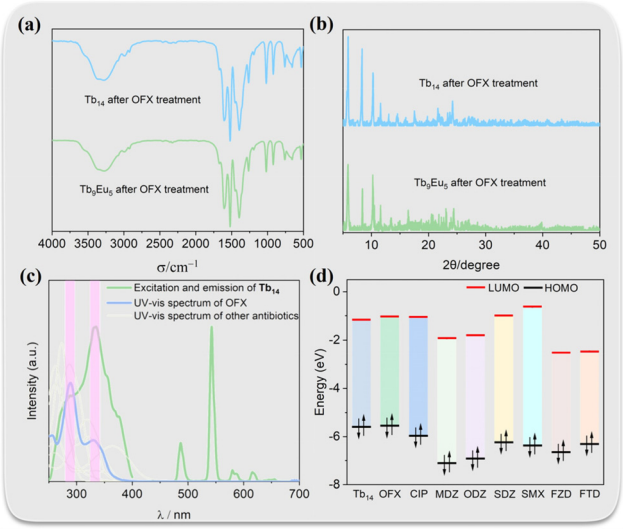

Fig. 7 (a) Infrared spectrum (b) and PXRD patterns of $\mathbf{Tb_{14}}$ after OFX treatment; (c) UV–vis absorption spectrum of antibiotics (C = 10^{-5} M) and excitation and emission spectra of $\mathbf{Tb_{14}}$ in water suspension; (d) HOMO and LUMO energies and isosurfaces for $\mathbf{Tb_{14}}$ and antibiotics.

transfer (FRET) mechanism. However, among the antibiotics tested, the excitation spectrum of $\mathbf{Tb_{14}}$ overlapped most effectively with the UV absorption spectrum of OFX, suggesting that OFX competes with Tb^{III} ions in $\mathbf{Tb_{14}}$ for the absorption of excitation light, leading to luminescence quenching, a phenomenon attributed to the internal filtration effect.[18,44]

The possibility of charge transfer was evaluated by comparing the frontier orbital energy levels of $\mathbf{Tb_{14}}$ and OFX using density functional theory (DFT) calculations (Fig. 7d). The results show that the LUMO level of $\mathbf{Tb_{14}}$ is higher than the HOMO level of OFX, and the HOMO level of $\mathbf{Tb_{14}}$ is lower than the LUMO level of OFX, indicating that charge transfer (CT) in the ground state is not feasible. However, since the HOMO level of OFX is higher than that of $\mathbf{Tb_{14}}$, photoinduced electron transfer (PET) may occur after the excitation of $\mathbf{Tb_{14}}$. Therefore, the luminescence quenching response of $\mathbf{Tb_{14}}$ to OFX may be attributed to the combined effects of the IFE and PET.

As for the possible sensing mechanism of $\mathbf{Tb_9Eu_5}$ towards OFX, the PXRD, IR, luminescence and UV-Vis absorption spectra of the complexes after the response show excellent consistency with the initial spectra, indicating that the structural integrity of $\mathbf{Tb_9Eu_5}$ is maintained after the identification of the target analyte (Fig. 7a, b and Fig. S28†). No new peaks were observed in all of these spectra, confirming that no new coordination bonds or hydrogen bonds were formed between $\mathbf{Tb_9Eu_5}$ and OFX, and ruling out the possibility of free Eu^{III} ions leaching from $\mathbf{Tb_9Eu_5}$ and forming a new complex with OFX that would enhance the red luminescence. Furthermore, as shown in the luminescence lifetime curve in Fig. S18,† the energy transfer efficiency from Tb^{III} to Eu^{III} is significantly enhanced after the addition of OFX. As the emission intensity of Tb^{III} weakens and that of Eu^{III} increases, a change in the emission color of $\mathbf{Tb_9Eu_5}$ is observed, shifting from yellow to red, which can easily be seen by the naked eye. Additionally, theoretical calculations revealed that the triplet energy level of OFX is 23 870 cm^{-1}, which is highly suitable for sensitizing the luminescence of Eu^{III} ions.[45] Therefore, the enhancement of red emission observed in the $\mathbf{Tb_9Eu_5}$ complex upon interaction with OFX can be partly attributed to the "antenna effect", where OFX acts as an energy donor, transferring energy to the Eu^{III} ions and thus amplifying their luminescence.

To further expand the application of Ln_{14} in OFX sensing and enhance the visualization and portability of the detection process, we developed a composite film sensor based on the combination of clusters and hydrogel. Specifically, we integrated Ln_{14} with an inexpensive, edible carrageenan hydrogel, taking advantage of its excellent water stability and luminescent properties. This approach led to the successful fabrication of a series of Tb_XEu_{14-X}@CRG composite films that display various colors under UV light (Fig. 8a). Taking the $\mathbf{Tb_9Eu_5}$**@CRG** film as an example, as shown in Fig. 9b–d, the film demonstrates a clear visual response to varying concentrations of OFX under 365 nm UV light. Initially emitting yellow in the absence of OFX, the film undergoes a noticeable shift to bright red luminescence after immersion in a 50 ppm OFX aqueous solution for 5 seconds. When exposed to a lower concentration of 20 ppm OFX for the same duration, the emis-

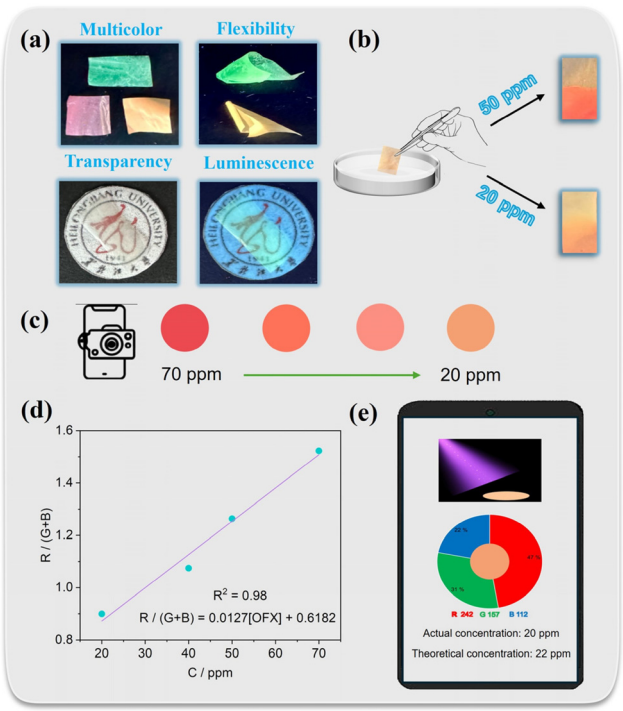

Fig. 8 (a) Advantages of composite film materials Tb_XEu_{14-X}@CRG; (b) luminescence changes of **Tb9Eu5@CRG** under 365 nm UV light after immersion in different concentrations of OFX aqueous solution; (c) color images of **Tb9Eu5@CRG** after immersion in OFX solutions of varying concentrations under 365 nm UV light; (d) linear relationship between color change (R/(G + B)) and OFX concentration; (e) schematic showing the detection of OFX using a smartphone device.

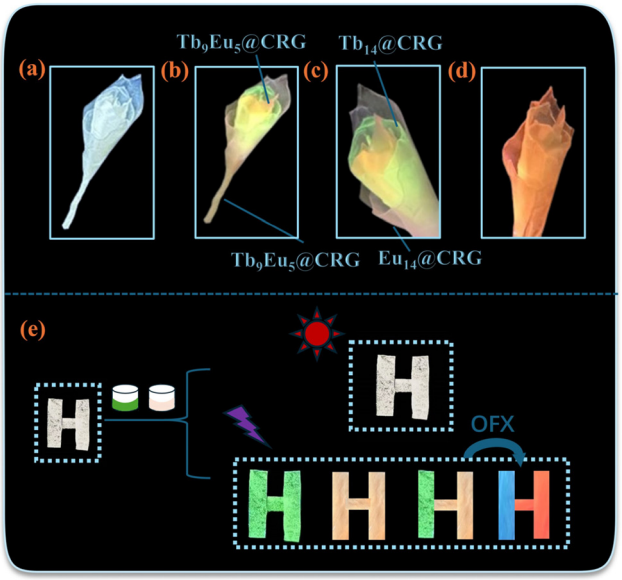

Fig. 9 (a) and (b) Photographs of an anti-counterfeiting pattern "Flower" taken before and after turning on the 365 nm UV light; (c) partial enlarged view of "Flower"; (d) photographs of "Flower" after immersion in 50 ppm OFX solution under 365 nm UV light; (e) pictures of the letter "H" stitched together using different colored hydrogel films in daylight and under 365 nm UV light.

sion transitions to an orange-yellow hue, reflecting its sensitivity to different OFX concentrations. Notably, the **Tb_9Eu_5@CRG** hydrogel membrane exhibits a detection limit for OFX as low as 20 ppm, which is significantly below the maximum residue limit of 90 ppm for quinolone drugs set by the European Union.[18]

Subsequently, **Tb_9Eu_5@CRG** was separately immersed in OFX solutions of varying concentrations, and its color change was observed under 365 nm UV light irradiation. As the OFX concentration fluctuated within the range of 20 ppm to 70 ppm, the luminescence emission intensity of **Tb_9Eu_5@CRG** undergoes corresponding changes. It is noteworthy that the luminescence emission photographs could be conveniently captured using a smartphone, and the corresponding RGB values were readily obtained *via* a commonly available application (as illustrated in Fig. 8c). Within the concentration range of 20 ppm to 70 ppm, a linear relationship was established between the $(R/(G+B))$ ratio and the OFX concentration, which can be utilized to accurately determine the OFX concentration in unknown samples (as depicted in Fig. 8d and e).

Anti-counterfeiting application

To harness the luminescent properties of the co-doped materials and composite films for practical applications, we devised two innovative anti-counterfeiting strategies leveraging their unique characteristics.

Strategy 1: by cutting films with varying emission colors, a variety of anti-counterfeiting patterns can be assembled. For example, a three-dimensional "Flower" was created through this approach, forming the first layer of security (Fig. 9a). The films, with different Tb^{III}/Eu^{III} ratios, emit distinct colors under 365 nm UV light, adding a second layer of protection (Fig. 9b). This method demonstrates an effective dual-layer anti-counterfeiting labeling strategy. Furthermore, immersing the "Flower" in a 50 ppm OFX solution for 5 seconds and then exposing it to 365 nm UV light caused the green luminescent areas to be quenched, resulting in a red emission overall (Fig. 9c and d).

Furthermore, an "H" character was designed using the same cutting and assembly technique. This pattern remained invisible under natural light but emitted green and orange luminescence under UV irradiation (Fig. 9e). Leveraging the luminescence response characteristics of Ln_{14} to OFX, OFX solution was sprayed onto the "H" pattern. The results demonstrated that, after application, the left side of the "H" experienced luminescence quenching, turning blue, while the right side exhibited enhanced luminescence, shifting to red. The distinct contrast in luminescence before and after the application of OFX was pronounced, and this localized variation further strengthened its utility as an anti-counterfeiting feature.

Strategy 2: by using the variations in the relative intensities of the distinct emission spectra of Tb_XEu_{14-X} clusters, optical barcode outputs can be created (Fig. S29†). From left to right, these bars correspond to the following transitions: $^5D_4 \rightarrow {}^7F_6$ (487 nm), $^5D_4 \rightarrow {}^7F_5$ (542 nm), $^5D_0 \rightarrow {}^7F_2$ (608 nm), and $^5D_0 \rightarrow {}^7F_4$ (698 nm). In these barcodes, green bars represent the emissions of Tb^{III}, while red bars indicate the emissions of Eu^{III}. And the inset displays photographs of the heterometallic clusters under UV lamp excitation, illustrating their respective emission colors. This tunability offers potential applications in constructing high-fidelity optical barcodes through color encoding.[16]

Conclusions

In summary, this study highlights the multifunctionality of lanthanide clusters in magnetic refrigeration, luminescence sensing, and anti-counterfeiting. Magnetic measurements reveal the weak antiferromagnetic interactions between Gd^{III} ions and the significant magnetocaloric effect of **Gd_{14}**. Photoluminescence experiments indicate that **Tb_{14}**, **Eu_{14}**, and **Sm_{14}** complexes exhibit characteristic emission properties, with tunable luminescence achieved through heterometallic doping. Most importantly, the study demonstrates that **Tb_9Eu_5** represents the first example of Ln-based cluster as a ratiometric luminescent probe for the detection of OFX. Furthermore, the composite film sensor demonstrates exceptional performance in visual detection and anti-counterfeiting applications. This work not only expands the application potential of lanthanide clusters but also provide innovative methodologies for material design and performance optimization in related technologies.

Author contributions

Tian-Tian Wang: synthesis, measurement, analysis and writing; Hao Wang: measurement and check writing; Wen-Bin Sun: supervision, discussion, writing – reviewing and editing.

Data availability

The authors confirm that the data supporting the findings of this article is given within this article and the ESI.†

Conflicts of interest

There are no conflicts to declare.

Acknowledgements

This work was supported by the NSFC (No. 22071047) and Natural Science Foundation of Heilongjiang Province (PL2024B013).

References

1 Z. Wang, Y. Du, C. Yang, X. Liu, J.-Q. Zhang, E.-H. Li, Q. Zhang and X.-L. Wang, Occurrence and ecological hazard assessment of selected antibiotics in the surface waters in and around Lake Honghu, China, *Sci. Total Environ.*, 2017, **609**, 1423–1432.
2 P. Kovalakova, L. Cizmas, T. J. McDonald, B. Marsalek, M. Feng and V. K. Sharma, Occurrence and toxicity of antibiotics in the aquatic environment: A review, *Chemosphere*, 2020, **251**, 126351.
3 X. Van Doorslaer, J. Dewulf, H. Van Langenhove and K. Demeestere, Fluoroquinolone antibiotics: An emerging class of environmental micropollutants, *Sci. Total Environ.*, 2014, **500–501**, 250–269.
4 J. Du, Q.-H. Liu, Y. Pan, S.-D. Xu, H.-X. Li and J.-H. Tang, The Research Status, Potential Hazards and Toxicological Mechanisms of Fluoroquinolone Antibiotics in the Environment, *Antibiotics*, 2023, **12**, 1058.
5 G. Carlucci, Analysis of fluoroquinolones in biological fluids by high-performance liquid chromatography, *J. Chromatogr. A*, 1998, **812**, 343–367.
6 S. Bhatt and S. Chatterjee, Fluoroquinolone antibiotics: Occurrence, mode of action, resistance, environmental detection, and remediation-A comprehensive review, *Environ. Pollut.*, 2022, **315**, 120440.
7 J. Wen, X.-D. Yao, S.-J. Geng, L.-J. Zhu, H. Jiang and L.-M. Hu, Urinary antibiotic levels and risk of overweight/obesity in preschool children: A biomonitoring-based study from eastern China, *Ecotoxicol. Environ. Saf.*, 2024, **269**, 115733.
8 R.-J. Gui, H. Jin, X.-N. Bu, Y.-X. Fu, Z.-H. Wang and Q.-Y. Liu, Recent advances in dual-emission ratiometric fluorescence probes for chemo/biosensing and bioimaging of biomarkers, *Coord. Chem. Rev.*, 2019, **383**, 82–103.
9 X.-Y. Pei, Y. Pan, L.-C. Zhang and Y. Lv, Recent advances in ratiometric luminescence sensors, *Appl. Spectrosc. Rev.*, 2021, **56**, 324–345.
10 X.-R. Chen, Q.-M. Yang, X.-Y. Lv, Y.-H. Xiong, T.-B. Zhong and X.-L. Huang, Rational design of ratiometric aggregation-induced emission luminogens for biosensing and bioimaging, *Coord. Chem. Rev.*, 2024, **516**, 215970.
11 J.-J. Hu, Y.-G. Li, H.-R. Wen, S.-J. Liu, Y. Peng and C.-M. Liu, Stable Lanthanide Metal–Organic Frameworks with Ratiometric Fluorescence Sensing for Amino Acids and Tunable Proton Conduction and Magnetic Properties, *Inorg. Chem.*, 2022, **61**, 6819–6828.
12 X.-Y. Qi, Y.-E. Zeng, X.-H. Diao, Y. Muhammad, C. Chen, H. Wang, W. Li and C.-S. Qi, Colorimetric fluorescence determination of anthrax biomarker using a bimetallic lanthanide metal–organic framework, *Polyhedron*, 2024, **248**, 116774.
13 D. Yang, S.-L. Mei, Z.-Q. Wen, X.-A. Wei, Z.-J. Cui, B.-B. Yang, C. Wei, Y. Qiu, M. Li, H. Li, W.-L. Zhang, F.-X. Xie, L. Wang and R.-Q. Guo, Dual-emission of silicon nanoparticles encapsulated lanthanide-based metal-organic frameworks for ratiometric fluorescence detection of bacterial spores, *Microchim. Acta*, 2020, **187**, 666.
14 Y.-F. Zhao and D. Li, Lanthanide-functionalized metal-organic frameworks as ratiometric luminescent sensors, *J. Mater. Chem. C*, 2020, **8**, 12739–12754.
15 F.-X. Zhang, J.-Y. Li, Z.-R. Zhao, F.-Q. Wang, Y.-Y. Pu and H.-L. Cheng, Mixed-LnMOFs with tunable color and white light emission together with multi-functional fluorescence detection, *J. Solid State Chem.*, 2019, **280**, 120972.
16 D. A. Gálico, A. A. Kitos, J. S. Ovens, F. A. Sigoli and M. Murugesu, Lanthanide-Based Molecular Cluster-Aggregates: Optical Barcoding and White-Light Emission with Nanosized $\{Ln_{20}\}$ Compounds, *Angew. Chem.*, 2021, **133**, 6195–6201.
17 A. Jafari, S. Vahid Niknezhad, M. Kaviani, W. Saleh, N. Wong, P. P. Van Vliet, C. Moraes, A. Ajji, L. Kadem, N. Azarpira, G. Andelfinger and H. Savoji, Formulation and Evaluation of PVA/Gelatin/Carrageenan Inks for 3D Printing and Development of Tissue-Engineered Heart Valves, *Adv. Funct. Mater.*, 2024, **34**, 2305188.
18 X.-L. Yu, A. A. Ryadun, D. I. Pavlov, T. Y. Guselnikova, A. S. Potapov and V. P. Fedin, Ln-MOF-Based Hydrogel Films with Tunable Luminescence and Afterglow Behavior for Visual Detection of Ofloxacin and Anti-Counterfeiting Applications, *Adv. Mater.*, 2024, **36**, 2311939.
19 S. Fateixa, R. S. Carvalho, A. L. Daniel-da-Silva, H. I. S. Nogueira and T. Trindade, Luminescent Carrageenan Hydrogels Containing Lanthanopolyoxometalates, *Eur. J. Inorg. Chem.*, 2017, **2017**, 4976–4981.
20 Y.-S. Zhang and A. Khademhosseini, Advances in engineering hydrogels, *Science*, 2017, **356**, eaaf3627.

21 J.-H. Li, A.-J. Liu, Y.-J. Ma, S.-D. Han, J.-X. Hu and G.-M. Wang, A large magnetocaloric effect in two hybrid Gd-complexes: the synergy of inorganic and organic ligands towards excellent cryo-magnetic coolants, *J. Mater. Chem. C*, 2019, **7**, 6352–6358.
22 Y. Zou, W. Lv, Z. Xue, J. Pan, X.-Y. Li and G.-M. Wang, Pentagram-type Ln_{15} (Ln = Dy, Tb, Eu, Sm, Ho) clusters with different anion templates: magnetic and luminescence properties, *Dalton Trans.*, 2022, **51**, 16383–16388.
23 X.-M. Luo, Z.-B. Hu, Q.-f. Lin, W. Cheng, J.-P. Cao, C.-H. Cui, H. Mei, Y. Song and Y. Xu, Exploring the Performance Improvement of Magnetocaloric Effect Based Gd-Exclusive Cluster Gd_{60}, *J. Am. Chem. Soc.*, 2018, **140**, 11219–11222.
24 Y.-Q. Zhai, W.-P. Chen, M. Evangelisti, Z. Fu and Y.-Z. Zheng, Gd-based molecular coolants: Aggregating for better magnetocaloric effect, *Aggregate*, 2024, **5**, e520.
25 X.-L. Li, L.-F. He, X.-L. Feng, Y. Song, M. Hu, L.-F. Han, X.-J. Zheng, Z.-H. Zhang and S.-M. Fang, Two chiral tetradecanuclear hydroxo-lanthanide clusters with luminescent and magnetic properties, *CrystEngComm*, 2011, **13**, 3643–3645.
26 R.-Y. Wang, D.-T. Song and S.-N. Wang, Toward constructing nanoscale hydroxo–lanthanide clusters: syntheses and characterizations of novel tetradecanuclear hydroxo–lanthanide clusters, *Chem. Commun.*, 2002, **4**, 368–369.
27 F.-S. Guo, J.-D. Leng, J.-L. Liu, Z.-S. Meng and M.-L. Tong, Polynuclear and Polymeric Gadolinium Acetate Derivatives with Large Magnetocaloric Effect, *Inorg. Chem.*, 2012, **51**, 405–413.
28 P. Pandey, D. Chauhan, M. G. Walawalkar, S. K. Gupta, F. Meyer, G. Rajaraman and R. Murugavel, Hourglass-Shaped Homo- and Heteronuclear Nonanuclear Lanthanide Clusters: Structures, Magnetism, Photoluminescence, and Theoretical Analysis, *Inorg. Chem.*, 2024, **63**, 11963–11976.
29 G. A. Bain and J. F. Berry, Diamagnetic Corrections and Pascal's Constants, *J. Chem. Educ.*, 2008, **85**, 532.
30 O. V. Dolomanov, L. J. Bourhis, R. J. Gildea, J. A. K. Howard and H. Puschmann, OLEX2: a complete structure solution, refinement and analysis program, *J. Appl. Crystallogr.*, 2009, **42**, 339–341.
31 L. Miao, C.-M. Liu and H.-Z. Kou, $\{GdIII_7\}$ and $\{GdIII_{14}\}$ Cluster Formation Based on a Rhodamine 6G Ligand with a Magnetocaloric Effect, *Molecules*, 2024, **29**, 389.
32 Y.-F. Bi, X.-T. Wang, W.-P. Liao, X.-W. Wang, R.-P. Deng, H.-J. Zhang and S. Gao, Thiacalix[4]arene-Supported Planar Ln_4 (Ln = TbIII, DyIII) Clusters: Toward Luminescent and Magnetic Bifunctional Materials, *Inorg. Chem.*, 2009, **48**, 11743–11747.
33 J.-B. Peng, Q.-C. Zhang, X.-J. Kong, Y.-P. Ren, L.-S. Long, R.-B. Huang, L.-S. Zheng and Z. Zheng, A 48-Metal Cluster Exhibiting a Large Magnetocaloric Effect, *Angew. Chem., Int. Ed.*, 2011, **50**, 10649–10652.
34 J.-B. Peng, X.-J. Kong, Q.-C. Zhang, M. Orendáč, J. Prokleška, Y.-P. Ren, L.-S. Long, Z. Zheng and L.-S. Zheng, Beauty, Symmetry, and Magnetocaloric Effect—Four-Shell Keplerates with 104 Lanthanide Atoms, *J. Am. Chem. Soc.*, 2014, **136**, 17938–17941.
35 J.-L. Liu, Y.-C. Chen and M.-L. Tong, Molecular Design for Cryogenic Magnetic Coolants, *Chem. Rec.*, 2016, **16**, 825–834.
36 S.-W. Zhang and P. Cheng, Coordination-Cluster-Based Molecular Magnetic Refrigerants, *Chem. Rec.*, 2016, **16**, 2077–2126.
37 Z.-M. Zhang, L.-Y. Pan, W.-Q. Lin, J.-D. Leng, F.-S. Guo, Y.-C. Chen, J.-L. Liu and M.-L. Tong, Wheel-shaped nanoscale 3d–4f $\{CoII_{16}LnIII_{24}\}$ clusters (Ln = Dy and Gd), *Chem. Commun.*, 2013, **49**, 8081–8083.
38 X.-Y. Zheng, J.-B. Peng, X.-J. Kong, L.-S. Long and L.-S. Zheng, Mixed-anion templated cage-like lanthanide clusters: Gd_{27} and Dy_{27}, *Inorg. Chem. Front.*, 2016, **3**, 320–325.
39 Q. Wang, S.-H. Lu, L.-X. Xu, J.-L. Wang, Y.-T. Yu, X. Bai, H. Mei and Y. Xu, $C_2O_4^{2-}$-templated cage-shaped Ln_{28} (Ln = Gd, Eu) nanoclusters with magnetocaloric effect and luminescence, *Inorg. Chem. Front.*, 2023, **10**, 4109–4116.
40 M.-Y. Wu, F.-L. Jiang, X.-J. Kong, D.-Q. Yuan, L.-S. Long, S. A. Al-Thabaiti and M. Hong, Two polymeric 36-metal pure lanthanide nanosize clusters, *Chem. Sci.*, 2013, **4**, 3104–3109.
41 S. S. Nagarkar, B. Joarder, A. K. Chaudhari, S. Mukherjee and S. K. Ghosh, Highly Selective Detection of Nitro Explosives by a Luminescent Metal–Organic Framework, *Angew. Chem., Int. Ed.*, 2013, **52**, 2881–2885.
42 C. Analytical Methods, Recommendations for the definition, estimation and use of the detection limit, *Analyst*, 1987, **112**, 199–204.
43 L. Wang, Y.-L. Zhu, T.-F. Zheng, Z.-H. Zhu, Y. Peng, Y.-Q. Wu, J.-L. Chen, S.-J. Liu and H.-R. Wen, A highly stable chain-based EuIII metal–organic framework as a turn-on and blue-shift luminescent sensor for dipicolinic acid, *Dalton Trans.*, 2023, **52**, 10567–10573.
44 X. Yu, A. A. Ryadun, D. I. Pavlov, T. Y. Guselnikova, A. S. Potapov and V. P. Fedin, Highly Luminescent Lanthanide Metal-Organic Frameworks with Tunable Color for Nanomolar Detection of Iron(III), Ofloxacin and Gossypol and Anti-counterfeiting Applications, *Angew. Chem., Int. Ed.*, 2023, **62**, e202306680.
45 X.-L. Leng, W.-X. Hao, X.-P. Yang, Z. Zhang, H. Li, Y.-A. Ma, Y.-B. Cheng and D. Schipper, Rapid and Reliable Excitation Wavelength-Dependent Detection of 2,6-Dipicolinic Acid Based on a Luminescent Cd(II)–Tb(III) Nanocluster, *Inorg. Chem.*, 2022, **61**, 8484–8489.

